J Mater Sci (2010) 45:4163–4173
DOI 10.1007/s10853-010-4506-4

Investigation of reactive cerium-based oxides for H_2 production by thermochemical two-step water-splitting

Stéphane Abanades · Alex Legal · Anne Cordier · Gilles Peraudeau · Gilles Flamant · Anne Julbe

Received: 11 January 2010 / Accepted: 8 April 2010 / Published online: 23 April 2010

Abstract This study focuses on the use of cerium-based mixed oxides for hydrogen production by solar-driven thermochemical two-step water-splitting. Mixed cerium oxides are proposed in order to decrease the reduction temperature of ceria and to avoid material sublimation occurring above 2,000 °C during the high-temperature solar step. Ceria-based nanopowders were synthesized by soft chemistry methods including the modified Pechini method. The influence of the synthesis method, the type of cationic element mixed with cerium, and the content of this added element was investigated by comparing the reduction temperatures of the derived materials. The synthesized powders were characterized by X-ray diffraction, thermogravimetric analysis, SEM, and Raman spectroscopy. Results showed that the synthesized pure cerium oxide is more reactive toward reduction than a commercial powder. Among the different elements added to ceria that were screened, the addition of zirconium significantly improved the reduction of ceria at temperatures below 1,500 °C. Increasing zirconium content further favored cerium reduction yield up to 70%. Water-splitting tests were performed to demonstrate the reactivity of the developed materials for H_2 production. The amount of H_2 evolved was enhanced with a temperature increase, the maximum H_2 production from $Ce_{0.75}Zr_{0.25}O_{2-\delta}$ was 0.24 mmol/g at 1,045 °C, and the powder reactivity upon cycling was demonstrated via thermogravimetry through two successive reduction–hydrolysis reactions.

S. Abanades (✉) · A. Legal · A. Cordier · G. Peraudeau · G. Flamant
Processes, Materials and Solar Energy Laboratory (PROMES-CNRS), 7 Rue du Four Solaire, 66120 Font Romeu, France
e-mail: Stephane.Abanades@promes.cnrs.fr; abanades@promes.cnrs.fr

A. Julbe
European Institute of Membranes (IEM), Place Eugène Bataillon, 34095 Montpellier Cedex 5, France

Introduction

The use of hydrogen as an environmentally friendly energy carrier is one of the most promising solutions to reduce emissions of greenhouse gases but also, ultimately, to replace fossil fuels whose stocks will tend to decrease. Depending on the feedstock, solar H_2 production processes can be divided into hybrid solar–fossil fuel processes involving the decarbonization and up-grading of carbonaceous materials (such as natural gas, coal, or biomass), and fully renewable processes based on water-splitting. Among the different production methods from water, the solar-driven thermochemical water-splitting cycles appear to be very attractive since resources, solar energy and water, are abundant and clean. In addition, they are potentially more efficient than electrolysis since the global solar-to-hydrogen energy efficiency is not limited by the intermediate conversion of heat to electricity. The two-step cycles consist of, first, the thermal reduction of the metal oxide using concentrated solar radiation as the source of high-temperature process heat (1) and second, the oxidation of the reduced oxide (or the metal) by water at moderate temperature (2):

$$M_xO_y \rightarrow M_xO_{y-z} + z/2O_2, \quad (1)$$

$$M_xO_{y-z} + zH_2O \rightarrow M_xO_y + zH_2. \quad (2)$$

The cycles based on ZnO/Zn or Fe_3O_4/FeO are currently the most largely studied. The ZnO/Zn cycle [1, 2] can theoretically produce a large amount of H_2 per gram of ZnO (12.3 mmol H_2/g). However, this large H_2 productivity is

limited by the partial recombination of Zn and O_2 during gas cooling after the reduction step. This drawback motivates studies on non-volatile materials. Fe_3O_4/FeO cycle [3–5] or doped ferrites [6] (MFe_2O_4 where M = Mn, Co, Ni, Cu, or Zn) are currently the most promising non-volatile cycles. They provide a significant reactivity with H_2O and a reasonable theoretical yield (4.3 mmol H_2/g of Fe_3O_4). However, since the reduction temperature is close to Fe_3O_4 melting point, significant sintering phenomena occur during the reduction step (1), which reduces the material performance [5].

A recent study of our group already highlighted the possibility of using the CeO_2/Ce_2O_3 cycle for H_2 production [7]. Ce_2O_3 shows a very good reactivity with water and the H_2 production yield is satisfactory (2.9 mmol H_2/g of CeO_2). This cycle, however, suffers from a partial sublimation of ceria at the reduction temperature (2,000 °C), which decreases the reduction yield. A similar system based on ceria was also proposed to produce syngas in the absence of a metal catalyst, and CH_4 in the presence of Ni, from H_2O and CO_2 [8].

This work, therefore, aims at studying alternative options to optimize this cycle based on the cerium oxide redox pair, in the presence of a judicious additive yielding the reduction step (1) at temperatures below the sublimation temperature. For this type of application, Kaneko et al. [9, 10] already showed that doping ceria by a lower valence cation can decrease the reduction temperature. However, such a doping promotes powder sintering. Miller et al. [6] also reported first results for both water and CO_2 splitting over a ceria/zirconia composition. Catalytic properties of ceria and ceria/zirconia systems were discussed extensively in [11]. When studying "three-way catalysts," Balducci et al. [12] demonstrated that zirconium addition favors the reduction of ceria and improves its thermal stability. In this study, the redox properties of cerium-based mixed oxides are applied to the splitting of water targeting H_2 production. In order to improve the reduction rate and thus to decrease the necessary temperature of ceria reduction for a given conversion, the following two options are combined: (1) the synthesis of nanopowders to increase the specific surface area and thus to favor the reduction at the particle surface, and (2) the addition of cationic elements in ceria with a valence lower or equal to that of cerium(IV) either to create oxygen vacancies or to warp the crystalline structure of ceria, which facilitates the volumetric diffusion of O^{2-} ions during the reduction within the particle volume. First, soft chemistry methods for nanopowders synthesis were considered and several mixed cerium oxides were screened to study the influence of the added element M (Al, Mn, Fe, Co, Cu, Zn, Zr) on the reduction of the mixed compound (CeO_2–MO_x). Then, a synthesis method was developed for preparing Zr-doped cerium oxide. The influence of the zirconium content was investigated by comparing the reduction of the derived materials. Finally, proof-of-principle water-splitting tests were carried out with the reduced samples for hydrogen production.

Experimental

Synthesis method

Pure ceria and a series of mixed oxide powders with molar formulation $(1-x)CeO_2-xZrO_2$ ($x = 0, 0.125, 0.25, 0.375$ and 0.5) were synthesized via a Pechini-derived polymeric route [13]. Cerium(III) nitrate hexahydrate (ALFA, purity > 99.5%) and zirconyl(IV) nitrate hydrate (ACROS, purity > 99.5%) were used as starting precursor salts. Stoichiometric amounts were dissolved in deionized water. Chelating and polymeric agents, hexamethylenetetramine, acetic acid, and acetylacetone, were added to the nitrate solution in order to form a resin. The mole ratio between organic compounds and cation was fixed at 3:1. The final solution (25 mL) was heated at 80 °C and stirred for 15 min. The sols were then dried and decomposed at 600 °C in air for 1 h to produce powders. Then, the obtained powders were ground and calcined in air for 2 h at 800 °C with a heating rate of 100 °C h^{-1}, in order to eliminate the organics. The yield of the synthesis was higher than 85%. The calcined powders were labeled *X*Zr*T*, where *X* is the Zr content (%) and *T* is the firing temperature (°C). The same procedure was also applied to synthesize the other mixed oxides CeO_2–MO_x with M = Al, Mn, Fe, Co, Cu, Zn, Zr3Y, Zr8Y (yttrium stabilized zirconia with 3 or 8% of yttrium).

Equipments for reduction and hydrolysis tests

The reduction reaction (1) of the oxide powders (350 mg for each sample) was studied by thermogravimetric analysis (TGA) (Setaram B70) in N_2 stream at 1,500 °C (heating rate of 30 °C/min, 5 h of dwell time). The reduction of larger samples (about 4 g in an alumina crucible) was also performed with a high-temperature tubular furnace (maximum temperature: 1,500 °C) swept by argon (0.2 NL/min) and coupled to an online trace oxygen analyzer (zirconium oxide sensor, O_2 range: 10–10,000 ppm, precision: 0.2%, calibration with 5,040 ppm O_2 in N_2). The O_2 concentration was thus monitored continuously during the progress of the reduction reaction. The H_2 production by water-splitting reaction (2) was studied as a function of temperature by using an experimental set-up consisting of a tubular quartz furnace fed with water steam (argon at 0.2 NL/min was used as carrier gas). The sample was first heated to the desired temperature in inert gas. Then, liquid water was injected inside the furnace by the means of a

peristaltic pump, water vaporized, and the resulting steam mole fraction was in the range 20–30%. Isothermal hydrolysis was performed. At the reactor exit, excess water was eliminated thanks to a bubbler and a desiccant column to protect the analytical instrument. An hydrogen analyzer (catharometer, measurement scale: 0–5%, precision: 1% of full scale) measured online the H_2 mol fraction at the exit of the hydrolysis reactor. The powder reactivity upon cycling was also studied with a specifically designed thermobalance (Setaram Setsys Evolution) coupled with a steam generator (argon at 40 °C with 80% of relative humidity). This device allowed the program of successive cycles consisting of a high-temperature reduction step in inert gas followed by an hydrolysis step in humid gas.

Characterization of powders

The crystallographic structure of powders, before and after reduction, was determined by X-ray diffraction (XRD) using a Philips PW 1820 diffractometer with the Cu$K\alpha$ radiation (αCu = 0.15418 nm, angular range = 20°–75° 2θ, steps = 0.02° 2θ, recording time = 2 s). XRD patterns were fitted using a Pearson VII function. Mean crystallite sizes of the cubic type (fluorite) structure were calculated by the Scherrer formula using the (111) diffraction peak.

The microstructure of the powders fired at 800 and 1,500 °C was observed by FESEM (Hitachi S4500).

The reduction of ceria was investigated by Raman spectroscopy at room temperature (Jobin–Yvon Labram 1B spectrometer), using a 632.8 nm He–Ne laser. In order to observe the weak peaks in the Raman spectra, the most intensive peak was fitted using a pseudo-Voigt function.

Results and discussion

Effect of the synthesis method on the reduction of pure ceria

Pure ceria ($X = 0$) was first synthesized and its characteristics were compared with those of a commercial powder (Aldrich, particle size < 5 μm, purity > 99.9%). FESEM images of the synthesized powder thermally treated at 800 °C are shown in Fig. 1a, b. This powder is composed of large oxide sheets that are characteristic of the synthesis method (Fig. 1a). These sheets are made of small grains (10–20 nm) more or less sintered (Fig. 1b).

X-ray diffraction patterns of the two powders are compared in Fig. 2. In both patterns, all the diffraction peaks can be assigned to pure cerium(IV) oxide (JCPDF: no. 81-0792), crystallized in the fluorite-type structure (space group Fm3m). The size of ceria crystallites in the synthesized powder, calculated by the Scherrer formula, is less than 15 nm for the powder heated at 600 °C (XRD pattern not displayed) and less than 50 nm for the powder heated at 800 °C.

The synthesized pure cerium oxide (0Zr800) was also characterized by Raman spectroscopy (Fig. 3a). The spectrum exhibits a strong band centered at 465 cm^{-1} that slightly broadens toward low frequencies and its full width at half maximum (FWHM) is 10 cm^{-1}. This peak corresponds to the F_{2g} symmetric breathing mode of O^{2-} anions around each Ce^{4+} cation.

In addition, a small shoulder was detected at about 400 and 570 cm^{-1} (inset Fig. 3a). It was reported in the literature that both the peak broadening and the weak satellite peak are due to either small crystallite sizes [14] or to crystal defects such as oxygen vacancies in the fluorite structure [15]. However, we did not detect any shift to low frequencies and any peak at 260 cm^{-1}, also characteristic of small particles (<20 nm) [15]. Considering the relatively large mean crystallite size calculated from XRD data, the slight peak broadening and its small shoulder reveal a very small proportion of nanoparticles (<20 nm) or crystal defects.

Both commercial and synthesized pure ceria were tested for thermal reduction (1) at 1,500 °C in N_2 atmosphere. TGA curves are shown in Fig. 4. The reduction of ceria starts at 1,150 °C for both powders. It is almost complete after a 2 h temperature plateau at 1,500 °C. The maximum weight loss is 0.36% for the commercial powder and 0.41% for the synthesized powder. The synthesized pure ceria is thus slightly more reactive than the commercial one (higher final reduction extent).

After 5 h treatment at 1,500 °C in N_2, the powder is composed of large sintered grains whose diameters are less than 2 μm in diameter (Fig. 1c). Pores of about 200 nm in diameter can be observed between these grains whose surface reveals parallel crystallization waves (Fig. 1d) converging toward grain boundaries.

X-ray diffraction pattern of 0Zr1500 corresponds to cerium(IV) oxide (Fig. 2c), without any significant peak shift in comparison with the pattern of 0Zr800 (Fig. 2b). However, an asymmetry of the diffraction peak toward small angles was detected (inset Fig. 2c), which could confirm the presence of Ce^{3+} with a higher ionic radius than Ce^{4+}. Indeed, it was shown in the literature [16] that $CeO_{2-\delta}$ keeps the fluorite-type structure for $\delta < 0.5$, and changes to the rhombohedric symmetry only above $\delta = 0.5$. Mean crystallite sizes calculated from the FWHM of the (111) peak were around 250 nm. This value is largely underestimated in comparison with the SEM observations (Fig. 1d). The enlargement of the FWHM of the (111) peak (peak asymmetry) may be more due to secondary phase(s) like $CeO_{2-\delta}$ than to small crystallites.

The Raman spectrum of 0Zr1500 (Fig. 3b) features the strong band characteristic of cerium(IV) oxide at 465 cm^{-1}.

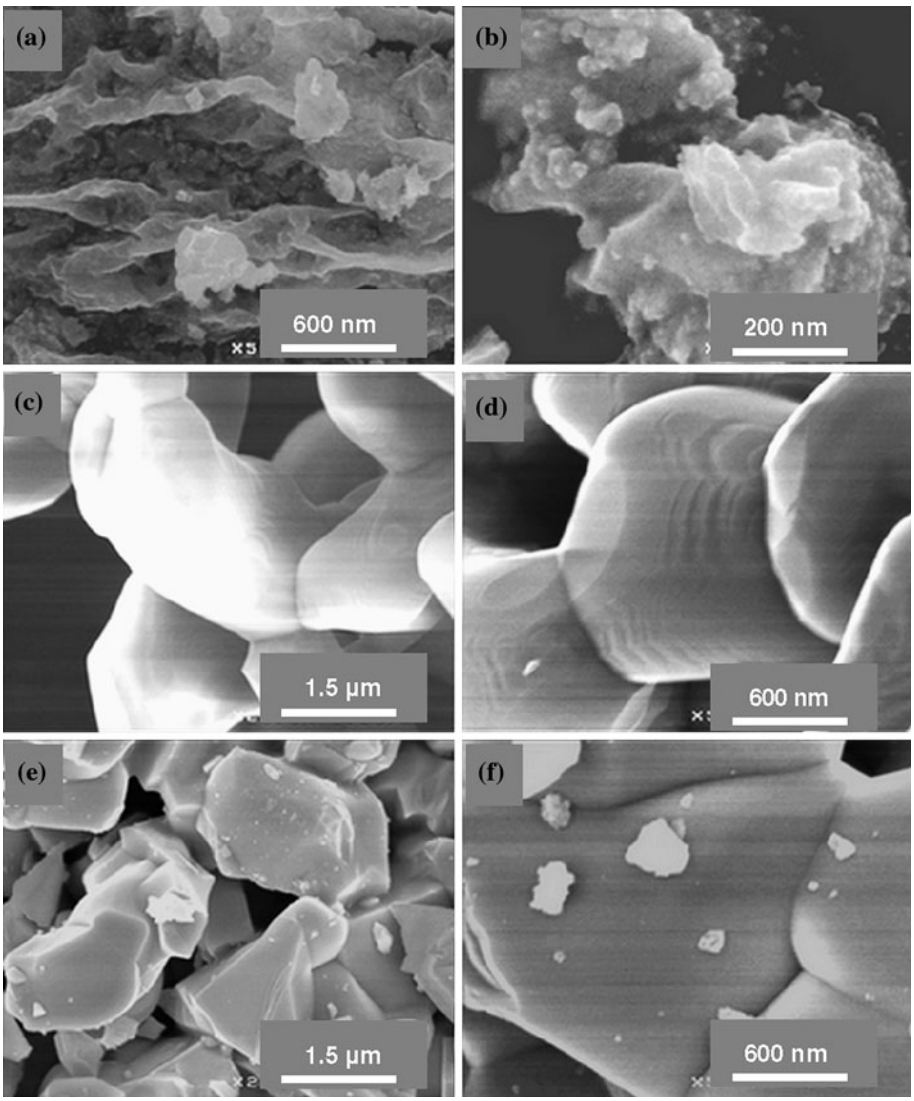

Fig. 1 SEM images of 0Zr800 (**a**, **b**), 0Zr1500 (**c**, **d**), and 25Zr1500 (**e**, **f**) powders

In addition, shoulders (stronger than for 0Zr800) are also observed at around 420 and 570 cm^{-1} (inset Fig. 3b), which can be attributed to the structural defects induced by the Ce^{3+} based secondary phase(s) [15].

Both Raman and XRD characterizations confirmed the presence of Ce^{3+} in the Pechini-derived ceria, after 5 h treatment at 1,500 °C in N_2 stream at atmospheric pressure. The synthesized ceria was more reactive than the commercial one. Although the reduction yield was relatively low (10%), no ceria was vaporized during the thermal treatment at 1,500 °C. This result is attractive in comparison with the previous studies [7] on CeO_2 thermal reduction under concentrated solar irradiation.

Effect of the kind of the added element on the reduction of ceria

The addition of a cationic element M^{y+} into ceria structure can be considered to favor oxygen ions mobility during the reduction of the material [9, 10]. This can be obtained by increasing the density of oxygen vacancies (case of M with a lower valence than Ce) or by reducing the distance between oxygen sites (case of M with the same valence but with a lower ionic radius than Ce). The elements considered were Al, Mn, Fe, Co, Cu, Zn, Zr, Zr3Y, Zr8Y (yttrium-stabilized zirconia with 3 or 8% of yttrium) and the atomic content of the element in the synthesized powders was set at 25%.

Zn was eliminated because of a strong vaporization during thermal treatment and it did not form a solid solution with ceria. In air, only the powders containing Cu and Co were reduced below 1,400 °C (mass loss observed in TGA). In N_2, mass losses were also measured for Zr, Zr3Y, Zr8Y in addition to Cu and Co. No mass loss was observed for Al, Mn, Fe, which means that a solid solution was not formed and the added element did not promote ceria reduction. Inversely, Kaneko et al. [10] produced $CeO_2-xFe_2O_3$ solid solution from a specific synthesis

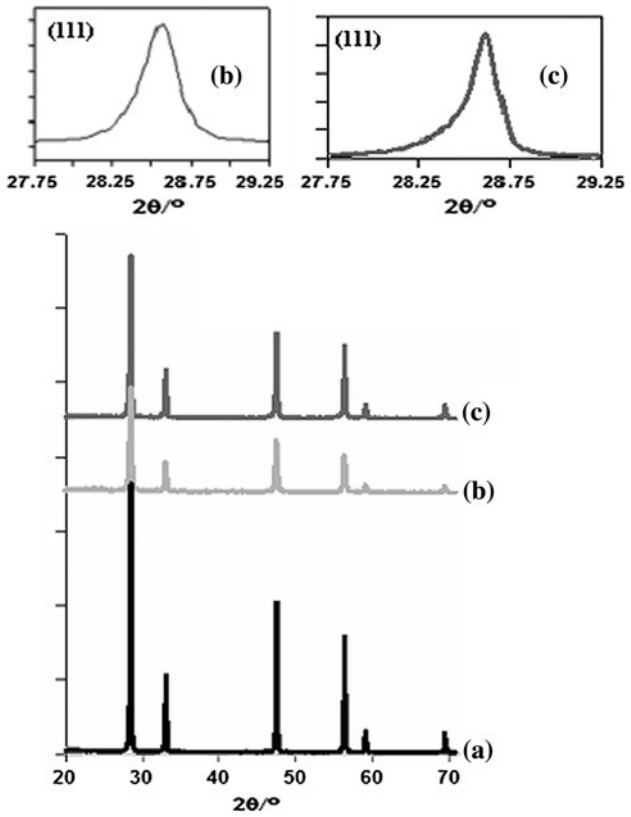

Fig. 2 XRD patterns of (*a*) Aldrich CeO_2 powder, (*b*) 0Zr800, and (*c*) 0Zr1500 powders

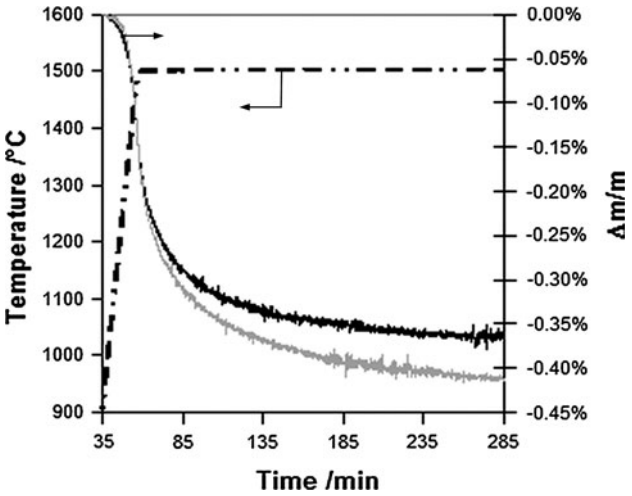

Fig. 4 TGA of commercial ceria (*continuous black line*) and 0Zr800 (continuous gray line) powders, and corresponding temperature profile (*dot line*)

method (urea–nitrate combustion method) and showed repeated O_2-releasing reduction at 1,400 °C and H_2 generation at 1,000 °C. For Cu and Co, XRD analysis showed the presence of CeO_2 coexisting with Cu_2O or CoO phases, which means that the mass losses were due to the reduction of CuO and Co_3O_4. The Raman spectrum of the reduced powders only consists of a large band centered at 465 cm^{-1} (FWHM: 55 cm^{-1}), which is characteristic of Ce(IV). Thus, the addition of Cu or Co did not favor the reduction of ceria. In addition, these Cu- and Co-based reduced powders are not reactive with water at 1,000 °C. Therefore, ceria reduction yielding Ce(III) species was obtained only in the case of Zr and yttrium stabilized zirconia. For these compounds, XRD shows the formation of solid solutions after thermal treatment at 1,400 °C in air, which is evidenced by a shift of the diffraction peaks toward high angles (decrease of the cell parameter because of the substitution of Ce^{4+} (0.092 nm) by Zr^{4+} (0.084 nm) with a smaller ionic radius). This shift is lowered when the sample is reduced in argon because the conversion of Ce^{4+} (0.092 nm) into Ce^{3+} (0.103 nm) generates an increase of the cell parameter of the fluorite structure and thus, a shift toward small angles that compensates the shift toward high angles due to the formation of a solid solution between cerium and zirconium oxides.

Effect of zirconium addition on the reduction of ceria

Solid solutions of cerium–zirconium oxides were prepared with Zr atomic content up to 50%. The XRD patterns of the powders prepared at 800 °C with different zirconium concentrations are shown in Fig. 5a. Several peaks (black arrows in Fig. 5a) can be assigned to the cubic ceria-type

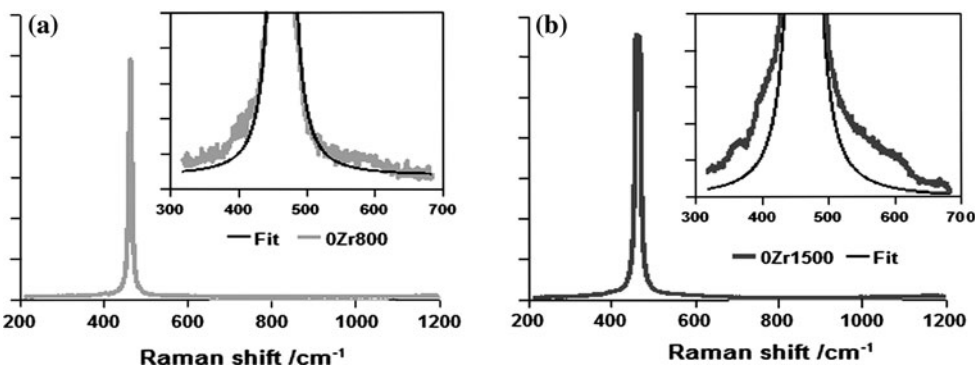

Fig. 3 Raman spectra of **a** 0Zr800 and **b** 0Zr1500 powders

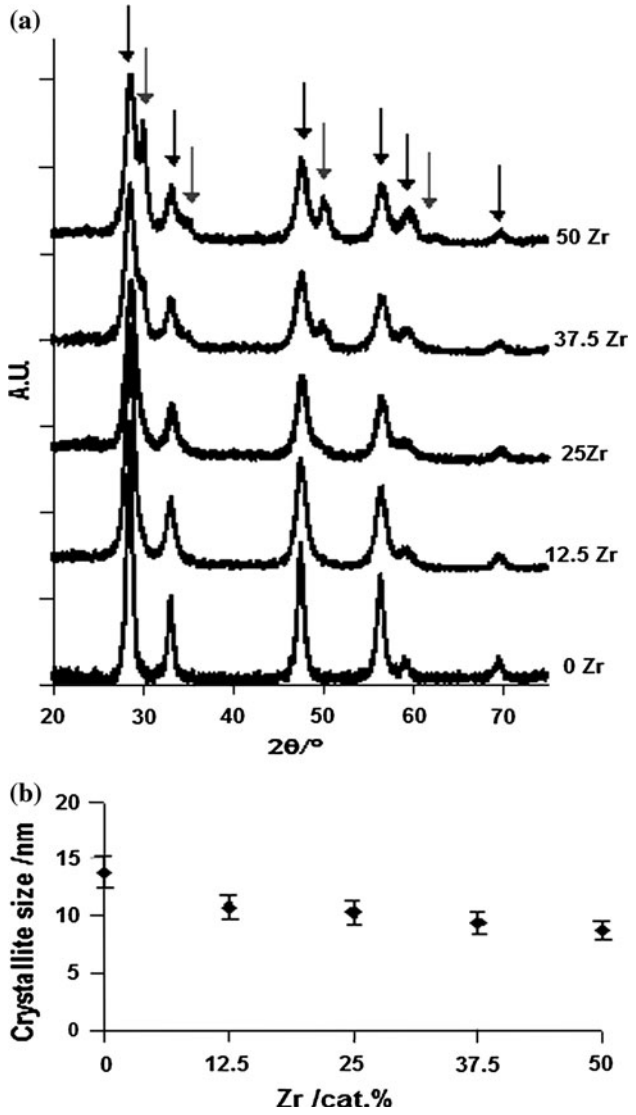

Fig. 5 **a** XRD patterns of XZr800 powders (*black and gray arrows* indicate the ceria-rich and zirconia-rich phases, respectively) and **b** corresponding evolution of the crystallites size versus *X*

structure (JCPDF: no. 81-0792). For 50Zr800 and 37.5Zr800 powders, an additional series of diffraction peaks (gray arrows in Fig. 5a) can be evidenced at 30.2°, 35.3°, 50.4°, and 61°. These peaks can be assigned to a tetragonal zirconia-type phase (space group P42/nmc, JCPDF: no. 82-1398). They are also detected in 25Zr800 and 12.5Zr800 powders. After heating at 800 °C, the powders thus consist of a mixture of a ceria-rich phase (cubic-type structure) with a zirconia-rich phase (tetragonal-type structure) [17]. The concentration of the tetragonal phase increases with *X*. These two phases are neither pure ceria nor pure zirconia. However, considering their poor crystallinity degree and the presence of phase mixtures, the exact proportion of tetragonal phase can be hardly determined as well as the cell parameter. The evolution of the mean crystallite size of the ceria-type structure in *X*Zr800 series is shown in Fig. 5b as a function of *X*. The mean crystallite size tends to decrease when *X* increases. This behavior is associated to the increasing amount of disorder induced by the insertion of Zr atoms in the cubic ceria structure.

The Raman spectra of 12.5Zr800 and 25Zr800 samples are shown in Fig. 6a. Both spectra are characterized by a strong band centered at 465 cm^{-1} and two shoulders at about 420 and 570 cm^{-1}. These shoulders are stronger than in the 0Zr800 sample because of the higher amount of defects in the doped ceria structure. The calculated FWHM were 13.6 and 16.8 cm^{-1} for 12.5Zr800 and 25Zr800 powders, respectively. According to Weber et al. [18], there is a linear relationship between FWHM and crystallite sizes, i.e., the higher the FWHM, the smaller the

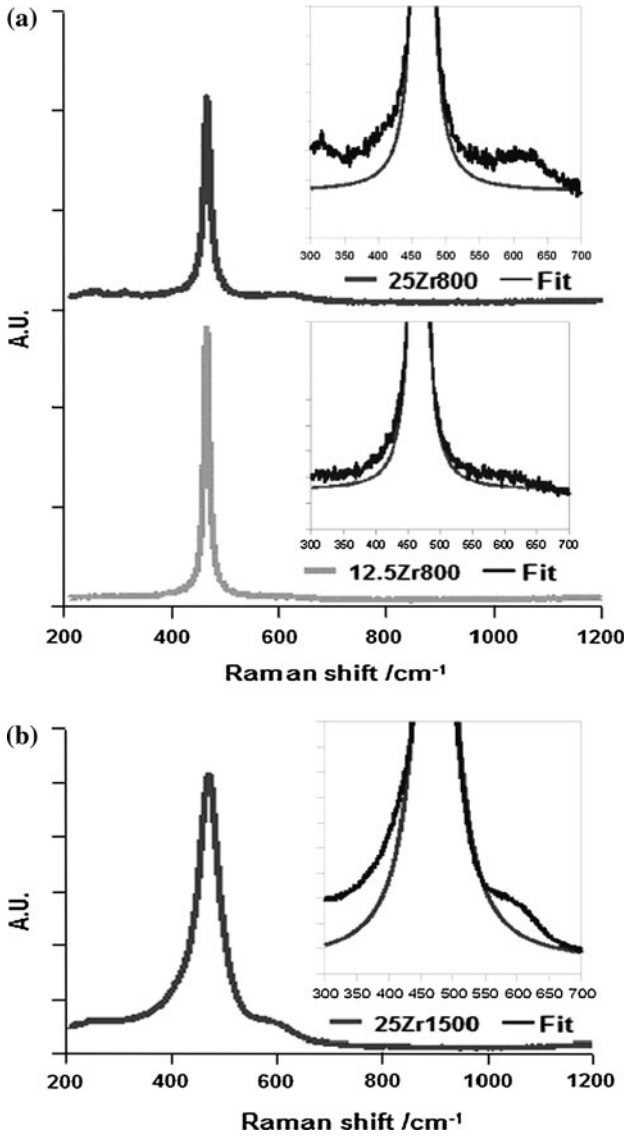

Fig. 6 Raman spectra of **a** 12.5Zr800 and 25Zr800 powders and **b** 25Zr1500 powder

crystallites. Consequently, the crystallite size of 25Zr800 is still smaller than the one of 12.5Zr800 even after heating at 800 °C. In addition, a band was detected at about 300 cm^{-1} in sample 25Zr800, which can be attributed to a displacement of oxygen atoms from tetrahedral to tetragonal sites [19]. This band, revealing traces of a tetragonal phase after heating at 800 °C, is not detected for the 12.5Zr800 sample.

The TGA curves of doped ceria powders in N_2 are shown in Fig. 7. When X increases, the temperature when the reduction starts decreases from 1,150 °C for $X = 0$ to 900 °C for $X = 50$. Moreover, the corresponding weight losses increase from 0.4 wt% ($X = 0$) to 1.9 wt% ($X = 50$).

In order to produce H_2, the Ce^{3+} species have to react with H_2O (reaction 2). Table 1 reports the reduction yield ($Ce^{3+}/(Ce^{3+}+Ce^{4+})$) and the quantity of Ce^{3+} per mole of oxide for each powder composition. Since no mass loss was observed during TGA in air at the reduction temperatures investigated, this means that volatilization did not occur and the mass loss in inert gas was only due to the O_2 release during reduction. The reduction yield reaches 70% for $X = 50$, whereas it is only 10% for $X = 0$. This result

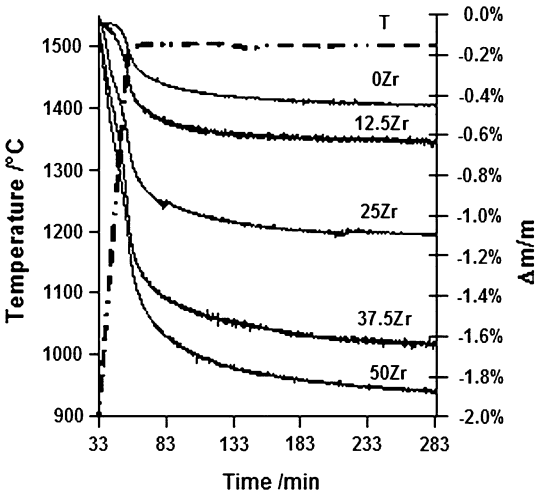

Fig. 7 TGA of *X*Zr800 powders (*continuous line*) and corresponding temperature profile (*dot line*)

Table 1 Reduction yield and absolute quantity of Ce^{3+} per mole of reduced oxide

Zr (mol.%) in ceria (X)	Ceria reduction yield (%)	Mol Ce^{3+}/mol oxide
0	10	0.10
12.5	15	0.13
25	29	0.22
37.5	51	0.32
50	70	0.35

confirms that Zr favors the reduction of cerium. The absolute quantity of Ce^{3+} per mole of oxide increases until X reaches 37.5 and then tends to stabilize around 0.35 for higher X values. In addition, it should be noted that the reduction conditions are not optimized in the TGA cell. Indeed, higher reaction yields may be expected by improving gas transfer to/from the reactive oxide surface, although the asymptotic like behavior of the curves in Fig. 7 suggests that any gain would be minimal. An adapted shaping of the powder as thin films on porous ceramic support could be an attractive option. The reactivity of CeO_2–ZrO_2 solid solutions in the O_2-releasing reaction increased with an increase in the content of Zr^{4+}. This reactivity increase may stem from relaxing the distortion of fluorite structure lattice caused by reduced Ce^{3+} ions with smaller Zr^{4+} ions. A part of Ce^{4+} is reduced to Ce^{3+} with a larger ionic radius and the increase in the content of Ce^{3+} results in the distortion of fluorite structure lattice. Zr^{4+} with the smallest ionic radius can relief the expansion of fluorite structure lattice due to the reduction of Ce^{4+}.

After the thermal treatment at 1,500 °C in N_2, the 25Zr1500 powder was observed by FESEM. It is composed of large sintered grains whose sizes are similar to those of pure ceria samples (0Zr1500) (Fig. 1e). In this powder that looks dense, no crystallization waves were observed on the grains (Fig. 1f).

The corresponding XRD patterns of the powders after thermal treatment at 1,500 °C are shown in Fig. 8a. All the diffraction peaks correspond to the fluorite-type structure, without any remaining trace of the tetragonal-type structure. Zirconium oxide and cerium oxide thus form a solid solution that crystallizes in the fluorite-type structure. A shift toward high angles is observed when X increases. This shift is attributed to the decreasing cell parameter due to the smaller ionic radius of zirconium compared to the cerium one. By fitting the (111) peak of the XRD patterns (Fig. 8b), we evidenced that it is actually composed of two peaks. The one on the right side (peak #2 centered at $2\theta = 29.1753 \pm 0.0949$) is attributed to the solid solution $Zr_xCe_{(1-x)}O_2$ and the one on the left side (peak #1 at $2\theta = 29.0844 \pm 0.1318$) is attributed to a reduced solid solution $Zr_xCe_{(1-x)}O_{2-\delta}$. Colon et al. [20] also suggest a demix of phases upon high-temperature aging. As 70% of cerium is reduced and as the highest peak is the right one (smaller cell parameter), the presence of these two peaks is mainly attributed to heterogeneities of zirconium concentration in the fluorite structure. In our case, it is not possible to directly link the (111) peak position with the amount of Zr in the fluorite cell because the right shift toward high angles is in part counterbalanced by a left shift toward small angles due to the presence of reduced cerium. According to previous conclusions and FESEM observations, the

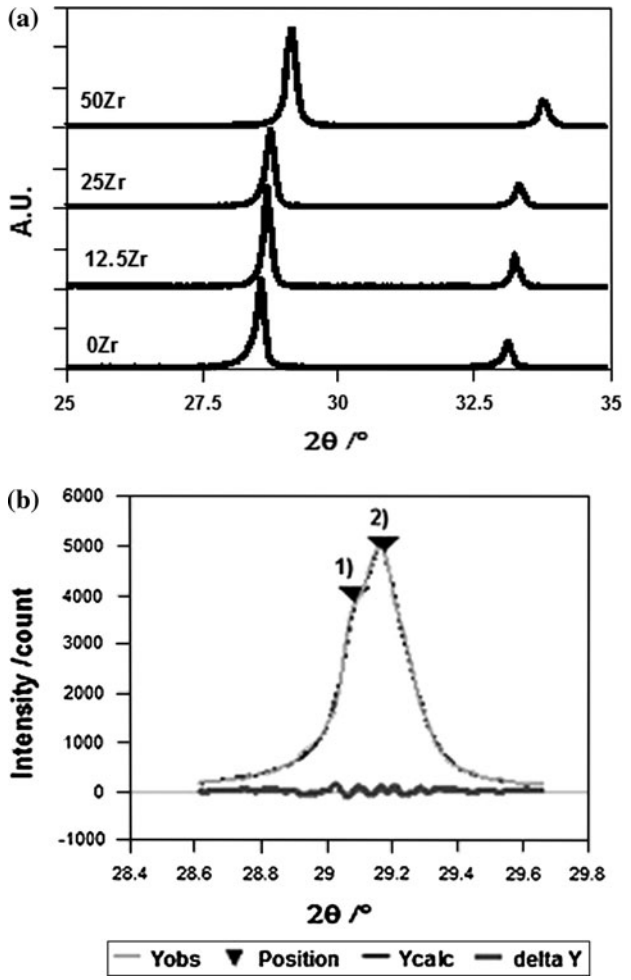

Fig. 8 **a** XRD patterns of *X*Zr1500 powders and **b** fitting of the double peak for the 50Zr1500 sample

FWHM broadening of the (111) peak of the powders is thus more due to the secondary phase(s) than to the effect of small crystallites.

The Raman spectrum of the 25Zr1500 sample is shown in Fig. 6b. The strongest band is centered at 472 cm^{-1}, i.e., shifted to higher frequency in comparison with previous samples. This shift was already reported in the literature for ceria–zirconia solid solution [21]. Two weak bands at about 420 and 570 cm^{-1} are also detected, which are characteristic of reduced cerium in significant quantity (in agreement with TGA). The FWHM was relatively large (53.5 cm^{-1}), but according to FESEM observations, this broadening cannot be attributed to small nanocrystallites, as suggested by Weber et al. [18], but rather to high density of structural defects in the sample [22]. In comparison with the 25Zr800 sample (Fig. 6a), the band broadening does not result only from the structural defects generated by Zr atoms in the ceria structure, but mostly from the higher concentration of Ce^{3+}.

In summary, TGA showed that it is possible to reduce $Ce_{1-x}Zr_xO_2$ below 1,500 °C in N_2 at atmospheric pressure without any material losses caused by sublimation. The reduction yield increased with Zr content and Raman spectroscopy proved that Ce^{4+}/Ce^{3+} is the redox pair that occurs during this reduction. After the reduction step, the $Ce_{1-x}Zr_xO_{2-\delta}$ solid solution (fluorite-type structure) was the only phase detected by XRD.

Hydrogen production tests

A preliminary water-splitting test was performed with the $Ce_{0.5}Zr_{0.5}O_{2-\delta}$ powder reduced during TGA at 1,500 °C in N_2 (sample 50Zr1500). Although the oxidation reaction of the mixed oxide required a temperature higher than 700 °C, the oxidation reaction with H_2O was fast (7 min for achieving the reaction at 800 °C) and its kinetics increased with temperature. The total amount of H_2 produced after 3 min at 900 °C was 1.2 mL/g mixed oxide (i.e., 0.046 mmol/g oxide). This quantity was low in comparison with the previous study performed with Ce_2O_3 at hydrolysis temperatures in the range 400–600 °C [7]. However, this first hydrolysis test showed that the H_2 production from cerium–zirconium oxide solid solution is feasible.

Further work was thus achieved to better explore the potential of these attractive solid-oxide solutions for H_2 production without any sublimation or phase decomposition. A more representative sample was synthesized in large amount (4 g) with global composition $Ce_{0.75}Zr_{0.25}O_2$. This sample was then reduced at 1,450 °C (heating rate of 10 °C/min) for 2 h of dwell time by using a tubular furnace swept by argon. The oxygen released by the reaction was monitored continuously by a trace O_2 analyzer. The evolution of O_2 production and temperature versus time during reduction reaction is plotted in Fig. 9. The release of O_2 started at about 1,000 °C, the O_2 concentration increased when the temperature rose and a peak concentration was measured at about 1,430 °C (Fig. 9). The total amount of O_2 was thus quantified by integration (120 μmol/g) and the final reduction extent of the powder was deduced (10.27%). The reduced powder $Ce_{0.75}Zr_{0.25}O_{2-\delta}$ was then used to investigate the effect of temperature on the hydrolysis reaction producing H_2. Hydrolysis experiments were carried out at 845, 945, and 1,045 °C with 1 g of the reduced powder sample in each test. The tubular furnace was swept by a gas mixture containing argon and steam, and the H_2 concentration was measured online at the reactor outlet. As a result, the H_2 production rate and the amount of H_2 generated increased with temperature (Fig. 10). The final H_2 productivity, obtained by integrating the H_2 production rate versus time profiles, was 140 μmol/g at 845 °C, 168 μmol/g at 945 °C, and 238 μmol/g at 1,045 °C. The

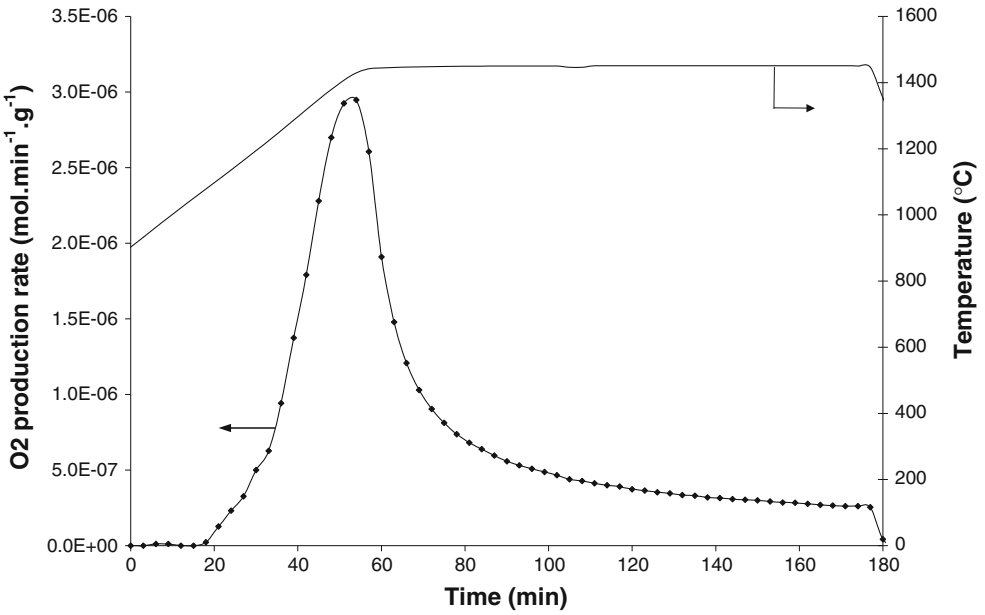

Fig. 9 O_2 production rate and temperature versus time during reduction of $Ce_{0.75}Zr_{0.25}O_2$ powder (4 g)

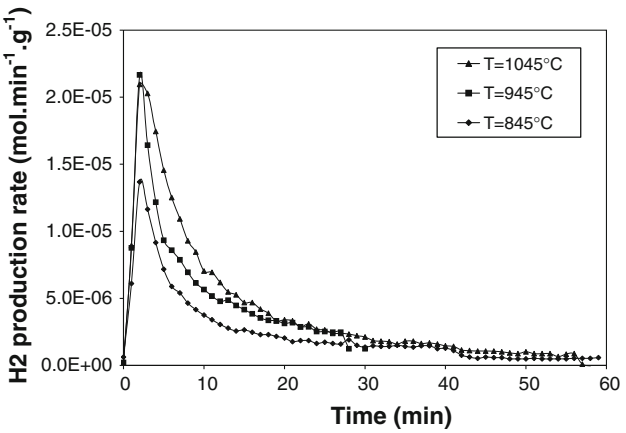

Fig. 10 H_2 production rate versus time during hydrolysis of $Ce_{0.75}Zr_{0.25}O_{2-\delta}$ powders

H_2/O_2 ratio thus approached 2 at the highest temperature investigated. One can notice that the O_2 production (Fig. 9) was slower than the H_2 production (Fig. 10). This is because the hydrolysis tests were performed in isothermal conditions (the reaction started once steam was injected at the desired temperature), while the O_2-releasing reaction occurred during sample heating and the reduction started at low temperature (about 1,000 °C) with a slow kinetic rate. The other reason is linked to the different main governing mechanisms. The O_2-releasing reaction is governed by ions diffusion inside the solid structure, whereas the H_2-generation reaction is governed by rapid particle surface reaction followed by internal gas diffusion in porous particle.

Finally, the reactivity of the synthesized material ($Ce_{0.75}Zr_{0.25}O_2$) upon cycling was investigated with a thermobalance coupled with a steam generator. The sample (162 mg) was placed in an alumina crucible and was subjected to the following temperature program that encompasses two complete cycles: (1) first reduction step in argon (20 mL/min): heating at 20 °C/min up to 1,450 °C, dwell time of 45 min, cooling down from 1,450 to 950 °C at 20 °C/min, (2) first hydrolysis step in argon + steam (80% of relative humidity at 40 °C): temperature plateau at 950 °C for 25 min, (3) second reduction step in argon (same as phase 1), (4) second hydrolysis step in argon + steam (same as phase 2). The time course of temperature and sample mass variation is represented in Fig. 11. During the first cycle (reduction at 1,450 °C and hydrolysis at 950 °C), the amounts of O_2 and H_2 produced were 138 and 162 μmol/g, respectively. These values are similar to the ones obtained with the experimental configurations in tubular furnace. The amounts of O_2 and H_2 produced were lower during the second cycle (86 and 89 μmol/g, respectively). The amount of H_2 produced in each cycle was estimated accounting for the sample mass uptake measured during the hydrolysis phase at 950 °C but also during the sample cool down preceding hydrolysis. Indeed, a sample mass increase was measured during the sample cool down from 1,450 to 950 °C in argon (Fig. 11), which can be attributed to the sample reoxidation with residual steam coming from the steam generator (RH between 3 and 5% even in dry argon). This mass uptake corresponds to about 30% of the total amount of H_2 produced. The mass transfer limitations between the gas phase and the particle surface must also be pointed out since they are not optimized in TGA crucible. The particles confined within the crucible naturally sit in small pile and diffusion

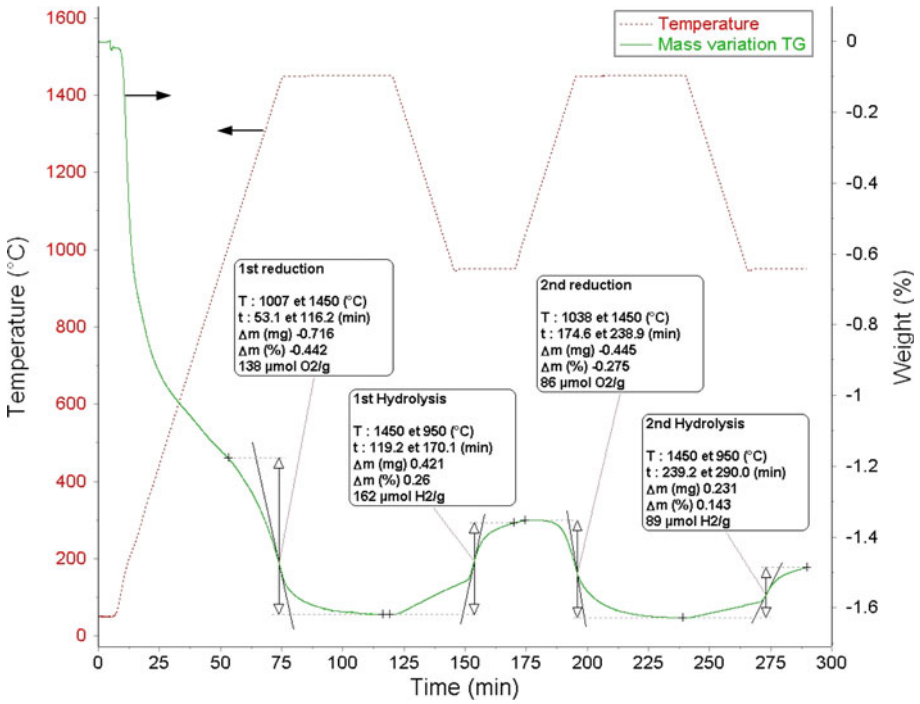

Fig. 11 TGA of a $Ce_{0.75}Zr_{0.25}O_2$ sample during two successive cycles

effects in the solid pile are important. The packing of the powder inside the crucible after the first cycle further enhanced the diffusion effects. As a result, the kinetic rate of the second hydrolysis was lowered markedly due to diffusion limitations inside the powder. This hydrolysis reaction was not finished and further H_2 could have been produced if the reaction duration was longer. An additional test in TGA was thus performed to illustrate the diffusion-controlled regime that settles during the second hydrolysis. A $Ce_{0.75}Zr_{0.25}O_{2-\delta}$ sample (172 mg) previously reduced in the tubular furnace at 1,450 °C for 2 h (Fig. 9) was first hydrolyzed at 950 °C for 45 min, then reduced at 1,450 °C for 45 min, and finally hydrolyzed again at 950 °C for 45 min (Fig. 12). The sample mass increased promptly

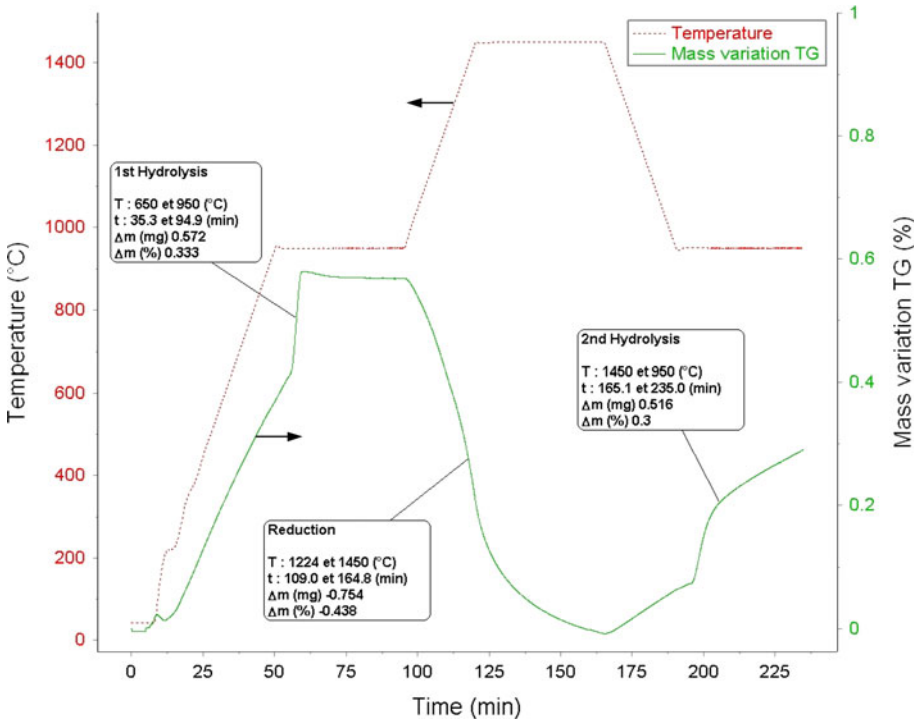

Fig. 12 TGA of $Ce_{0.75}Zr_{0.25}O_{2-\delta}$ powder previously reduced at 1,450 °C: sample mass variation and temperature during first hydrolysis at 950 °C for 45 min, reduction at 1,450 °C for 45 min, and second hydrolysis at 950 °C for 45 min

during the first hydrolysis as soon as steam was injected at 950 °C (amount of H_2 produced: 208 μmol/g), which denotes a reaction-controlled regime. The reduction reaction was then performed at 1,450 °C (amount of O_2 released: 137 μmol/g), which induced powder packing in the crucible. As a result of these physical limitations, the sample mass uptake during the second hydrolysis reaction (amount of H_2 produced: 188 μmol/g) was composed of a fast initial step followed by a diffusion-controlled step and H_2 production was still continuing after 45 min of reaction. Finally, the amounts of H_2 produced during the two hydrolysis reactions were close but the reaction rate decreased in the second hydrolysis due to diffusion limitations. These results thus confirmed that the synthesized material can be used in successive cycles without significant reactivity losses.

Conclusion

This work was carried out in order to decrease the reduction temperature of ceria below 1,500 °C in inert atmosphere at atmospheric pressure. The final targeted use of the reduced material is the hydrogen production from solar-driven two-step water-splitting.

The reduction of pure ceria synthesized by a modified Pechini method was first compared with the reduction of a commercial ceria powder. The nanosized crystallites of the synthesized powder led to a higher reduction yield than for the commercial powder. The addition of cationic elements into ceria structure was investigated and Zr (or yttrium stabilized zirconia) favored the reduction of ceria (formation of Ce(III) species).

The influence of zirconium addition (up to 50 mol.%) on the reduction yield of ceria mixed oxides was then studied. The higher the quantity of Zr, the lower the reduction temperature and the higher the reduction yield. Despite the non-optimized solid–gas exchange in TGA cell, a relatively high reduction yield of about 70% was obtained at 1,500 °C in N_2 for the highest Zr content (50 mol.%), and without any sublimation of the solid-oxide solution. The corresponding reduced mixed oxide contained 0.35 mol of Ce^{3+} per mole of mixed oxide.

Finally, this thermally reduced powder was tested for H_2 production by water-splitting. Although the oxidation reaction of the mixed oxide required a temperature higher than 700 °C, the redox reactivity of the ceria–zirconia solid-oxide solution was demonstrated for H_2 production by water-splitting. The material reactivity increased with temperature. A significant reactivity of $Ce_{1-x}Zr_xO_{2-\delta}$ was measured above 800 °C, which is a higher temperature than the hydrolysis temperature of Ce_2O_3. The H_2 productivity was about 0.24 mmol/g at 1,045 °C with a $Ce_{0.75}Zr_{0.25}O_{2-\delta}$ powder and the cycling capability of the material was demonstrated. Although the amount of H_2 produced was low compared to Ce_2O_3, it still can be optimized by adjusting the amount of Zr in the powder and it demonstrates that ceria–zirconia solid solutions are possible binary oxides candidates for H_2 production. Further work will be devoted to the improvement of phase transfer by powder shaping and to the development of a suitable solar reactor concept for achieving the two steps of the cycle repeatedly.

Acknowledgements The Energy Program of CNRS (CYCLHYSOL project, PE 3.1-1), the Agence Nationale de la Recherche (project ANR-09-JCJC-0004-01), and the CNRS Department of Engineering Sciences are gratefully acknowledged for financial support. The authors would like to thank E. Gerardin from IEM technical staff for her contribution in Raman and FESEM characterizations.

References

1. Steinfeld A (2002) Int J Hydrogen Energy 27:61
2. Weidenkaff A, Reller AW, Wokaun A, Steinfeld A (2000) Thermo Acta 359:69
3. Ehrensberger K, Frei A, Kuhn P, Oswald HR, Hug P (1995) Solid State Ion 78:151
4. Tamaura Y, Ueda Y, Matsunami J, Hasegawa N, Nezuka M, Sano T, Tsuju M (1999) Sol Energy 65:55
5. Tofighi A, Sibieude F (1984) Int J Hydrogen Energy 9:293
6. Miller JE, Allendorf MD, Diver RB, Evans LR, Siegel NP, Stuecker JN (2008) J Mater Sci 43:4714. doi:10.1007/s10853-007-2354-7
7. Abanades S, Flamant G (2006) Sol Energy 80:1611
8. Chueh WC, Haile SM (2009) ChemSusChem 2:735
9. Kaneko H, Miura T, Ishihara H, Taku S, Yokoyama T, Nakajima H, Tamaura Y (2007) Energy 32:656
10. Kaneko H, Ishihara H, Taku S, Naganuma Y, Hasegawa N, Tamaura Y (2008) J Mater Sci 43:3153. doi:10.1007/s10853-008-2499-z
11. Trovarelli A (2002) Catalysis by ceria and related materials. Imperial College Press, London
12. Balducci G, Kašpar J, Fornasiero P, Graziani M, Islam MS, Gale JD (1997) J Phys Chem B 101:1750
13. Pechini MP (1967) US Patent #3.330.697, 11 July 1967
14. Graham GW, Weber WH, Peters CR, Usman R (1991) J Catal 130:310
15. McBride JR, Haas KC, Poindexter BD, Weber WH (1994) J Appl Phys 76:2435
16. Kümmerle EA, Heger GJ (1999) Solid State Chem 147:485
17. Duran P, Gonzalez M, Moure C, Jurado JR, Pascual C (1990) J Mater Sci 25:5001. doi:10.1007/BF00580121
18. Weber WH, Haas KC, McBride JR (1993) Phys Rev B 48:178
19. Yashima M, Arashi H, Kakihana M, Yoshimura M (1994) J Am Ceram Soc 77:1067
20. Colon G, Pijolat M, Valdivieso F, Vidal H, Kaspar J, Finocchio E, Daturi M, Binet C, Lavalley JC, Baker RT, Bernal S (1998) J Chem Soc Faraday Trans 94:3717
21. Vidal H, Bernal S, Kašpar J, Pijolat M, Perrichon V, Blanco G, Pintado JM, Baker G, Colon RT, Fally F (1999) Catal Today 54:93
22. Otake T, Yugami H, Naito H, Kawamura K, Kawada T, Mizusaki J (2000) Solid State Ion 135:663